Journal of Materials Chemistry A

ROYAL SOCIETY OF CHEMISTRY

PAPER

View Article Online
View Journal



Cite this: DOI: 10.1039/d5ta05852j

# Atomically precise $Au_{42}$ and Cu-doped $Au_{42}$ nanorods for $CO_2$ reduction: the critical role of ligand removal

Rahul Somni,[a] Anik Sarkar,[b] Lianshun Luo,[c] Rongchao Jin,[c] Gangli Wang *[b] and Guoxiang Hu *[ad]

Atomically precise nanoclusters (APNCs) of coinage metals provide a powerful platform for elucidating structure–property relationships in catalysis due to their well-defined atomic structures. In this study, we investigate the electrocatalytic behavior of the rod-shaped $Au_{42}(SR)_{32}$ nanocluster and its copper-doped derivatives for the carbon dioxide reduction reaction ($CO_2RR$) and competing hydrogen evolution reaction (HER). By integrating density functional theory (DFT) calculations with electrochemical measurements, we demonstrate that ligand removal has a profound impact on catalytic activity and selectivity by altering the nanocluster's electronic structure and active sites. Among the ligand-modified configurations, the −SR removed $Au_{42}(SR)_{32}$ nanocluster exhibits the most favorable $CO_2RR$ performance, with significantly lower overpotentials and enhanced selectivity. While Cu doping can improve activity and selectivity in the pristine and −R removed nanoclusters, it reduces performance in the −SR removed nanocluster due to a shift in the potential-determining step (PDS) from *COOH formation to *CO desorption after Cu doping. The DFT predicted onset potentials for $CO_2RR$ and HER show excellent agreement with electrochemical experiments. Additionally, X-ray photoelectron spectroscopy (XPS) analysis confirms ligand stripping during reductive electrolysis. While site specific Cu doping remains to be achieved experimentally, our findings underscore the critical role of dynamic ligand behavior under operating conditions in the rational design of high-performance APNC-based electrocatalysts for $CO_2$ conversion.

Received 20th July 2025
Accepted 24th November 2025

DOI: 10.1039/d5ta05852j

rsc.li/materials-a



## Introduction

The electrochemical carbon dioxide reduction reaction ($CO_2RR$) offers a promising route and sustainable solution to produce value-added carbon-based fuels while mitigating rising atmospheric $CO_2$ levels.[1–4] Given the chemical inertness of the $CO_2$ molecule, efficient catalysis is essential. $CO_2RR$ catalysts must exhibit not only high activity and product selectivity but also a strong ability to suppress the competing hydrogen evolution reaction (HER). Meeting these criteria requires a detailed understanding of the energetics of reaction intermediates in multi-step processes involving multi-electron transfer, many of which are coupled with proton transfer.[5,6] Identifying the catalytically active sites is therefore crucial, yet remains challenging for conventional nanomaterial catalysts due to their polydispersity and lack of atomic-level structural uniformity.

In contrast, ultrasmall atomically precise nanoclusters (APNCs) have emerged as a powerful class of materials for catalysis.[7–13] These APNCs, typically 1–3 nm in size and consist of tens to hundreds of metal atoms, are protected by a monolayer of organic ligands and possess well-defined, crystallographically resolvable atomic structures. Their compositional tunability and molecular precision make them excellent platforms for bridging experimental and computational studies, enabling the correlations of mechanistic insights with catalytic activities at the atomic level.[11,14,15] Moreover, APNCs can be precisely doped with heteroatoms to form alloy-like structures not readily attainable *via* traditional colloidal synthesis.[16–20]

Among APNCs, thiolate-protected Au nanoclusters have demonstrated promising $CO_2RR$ activity.[21,22] While maintaining the inherent CO selectivity of bulk Au, these APNCs also exhibit unique interactions with $CO_2$ not observed on extended Au surfaces. For instance, the spherical $Au_{25}(SR)_{18}$ nanocluster shows improved $CO_2RR$ performance compared to bulk Au and larger Au nanoparticles, featuring lower overpotentials and higher faradaic efficiencies.[22,23] A newer member of the APNCs, the rod-shaped $Au_{42}(SR)_{32}$ nanocluster, features a hexagonally

[a]School of Chemistry and Biochemistry, Georgia Institute of Technology, Atlanta, GA 30332, USA
[b]Department of Chemistry, Georgia State University, Atlanta, GA 30303, USA. E-mail: glwang@gsu.edu
[c]Department of Chemistry, Carnegie Mellon University, Pittsburgh, PA 15213, USA
[d]School of Materials Science and Engineering, Georgia Institute of Technology, Atlanta, GA 30332, USA. E-mail: emma.hu@mse.gatech.edu

close-packed $Au_{20}$ kernel protected by two pairs of interlocked $Au_4(SR)_5$ staples at the ends and six $Au(SR)_2$ monomers along its body (Fig. 1a).[24] This anisotropic structure is unique in introducing one-dimensional character in its local electronic environment that should affect $CO_2$ adsorption and intermediate binding.

In this study, we investigate the electrocatalytic performance of rod-shaped $Au_{42}(SR)_{32}$ nanocluster and its Cu-doped derivatives for $CO_2$RR and HER. Cu is the only known metal that can catalyze $CO_2$RR to $C_{2+}$ products in appreciable yields.[25–31] Previous studies have shown that Cu doping in Au-based catalysts can enhance $CO_2$RR activity while suppressing HER.[32,33] As site specific Cu doping remains to be achieved experimentally, we explore potential doping sites in the $Au_{42}(SR)_{32}$ nanocluster by performing density functional theory (DFT) calculations, and assess how Cu incorporation affects the activity of $CO_2$RR and HER. The impacts of ligand removal,[34,35] a phenomenon that plays critical roles on the active sites and catalytic mechanism, are revealed for both pristine and Cu-doped $Au_{42}(SR)_{32}$ nanoclusters.

## Results and discussion

We first estimate the HOMO–LUMO gap of the $Au_{42}(SR)_{32}$ nanocluster using DFT. The structural model was based on available crystallographic data, as illustrated in Fig. 1a. To reduce computational cost without significantly affecting the electronic structure, the phenyl groups on the thiolate ligands were replaced with methyl groups.[36] Additional computational parameters and methods are provided in the SI. The DFT-calculated HOMO–LUMO gap is 1.09 eV. From experimental measurements using cyclic voltammetry (CV) and differential pulse voltammetry (DPV) shown in Fig. 1b, the first major anodic and cathodic peaks in CV correspond to the well-defined oxidation and reduction peaks at $0.92_9$ V and $-0.56_4$ V in DPV respectively (as indicated by the red asterisk in Fig. 1b). Additional redox features at higher potentials are poorly defined in CV but clearly revealed in DPV. Average of the first peak spacings, gaps after the first oxidation and reduction peaks indicated by the green arrows, $0.26_3$ and $0.31_4$ respectively, is used to estimate the capacitive charging energy of 0.28 eV corresponding to the gain or loss of 1e as described in concentric sphere model.[37] The experimental HOMO–LUMO gap by electrochemistry is determined to be 1.21 eV (0.69–(−0.80)–0.28). This value is in close agreement with the DFT prediction, thereby supporting the reliability of our computational model and providing confidence in the theoretical framework used to analyze the electronic structure and catalytic performance of the $Au_{42}(SR)_{32}$ nanocluster.

A signature redox activity of Au APNCs is the quantized double layer charging, featuring largely evenly spaced peak(s) in DPV upon further oxidation or reduction. Those indicate chemically and often electrochemically reversible redox behaviors within mild potential ranges owing to their intrinsic structural stability.[38,39] However, the $Au_{42}(SR)_{32}$ nanocluster exhibits chemical irreversibility upon the first oxidation and reduction. As shown in Fig. 2a and b, a weak reversal oxidation peak, circled in red, was only detectable at higher scan rates. This is a characteristic chemical irreversible reaction following electron reduction to LUMO, suggesting a sluggish ligand detachment rate in the order of sub-seconds upon reduction qualitatively. No reversal reduction feature is observed after the oxidation of HOMO, indicating a greater instability of the oxidized species. These observations reveal that both electron addition and removal destabilize the $Au_{42}(SR)_{32}$ nanocluster, potentially triggering structural rearrangements such as ligand loss. Reductive electrolysis at −0.78 V *vs.* RHE for 60 minutes was then performed on the $Au_{42}(SR)_{32}$ nanocluster for X-ray photoelectron spectroscopy (XPS) characterizations[40] (Fig. S5). Compared to the strong Au signals, the S signal decreased after electrolysis to below the threshold S/N ratio for quantitation. Semi-quantitatively, about 50% of the original 32 SR ligands remain detectable. Multi-cycle CVs of the $Au_{42}(SR)_{32}$ nanocluster film on electrode are included in Fig. S3. The shoulder

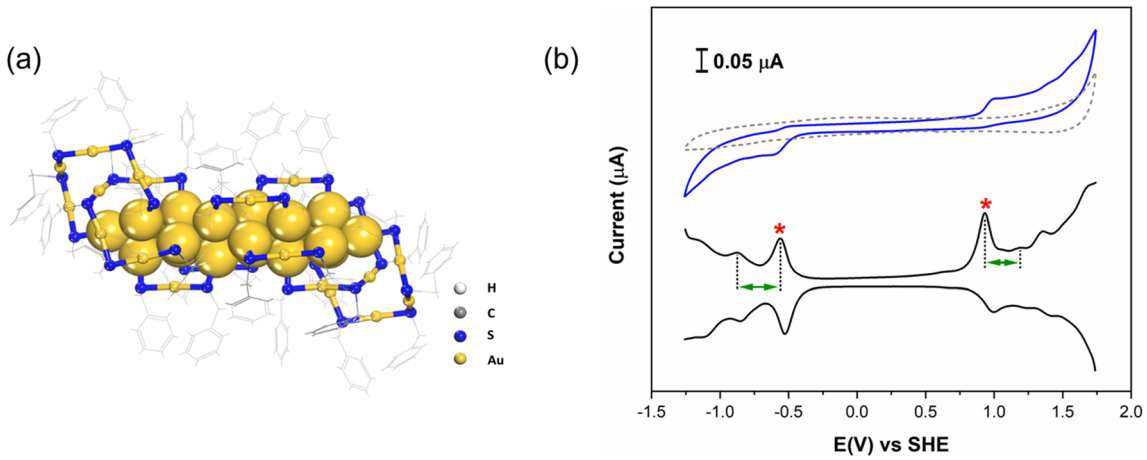


Fig. 1 (a) Atomic structure of the $Au_{42}(SR)_{32}$ nanocluster (SR = 2-phenylethanethiolate). Au atoms are shown in yellow, S in blue, and C in gray. (b) Cyclic voltammogram (top) and differential pulse voltammogram (bottom) of the $Au_{42}(SR)_{32}$ nanocluster. Dashed line in the CV was collected without the $Au_{42}(SR)_{32}$ nanocluster under otherwise identical condition as background for comparison.

 

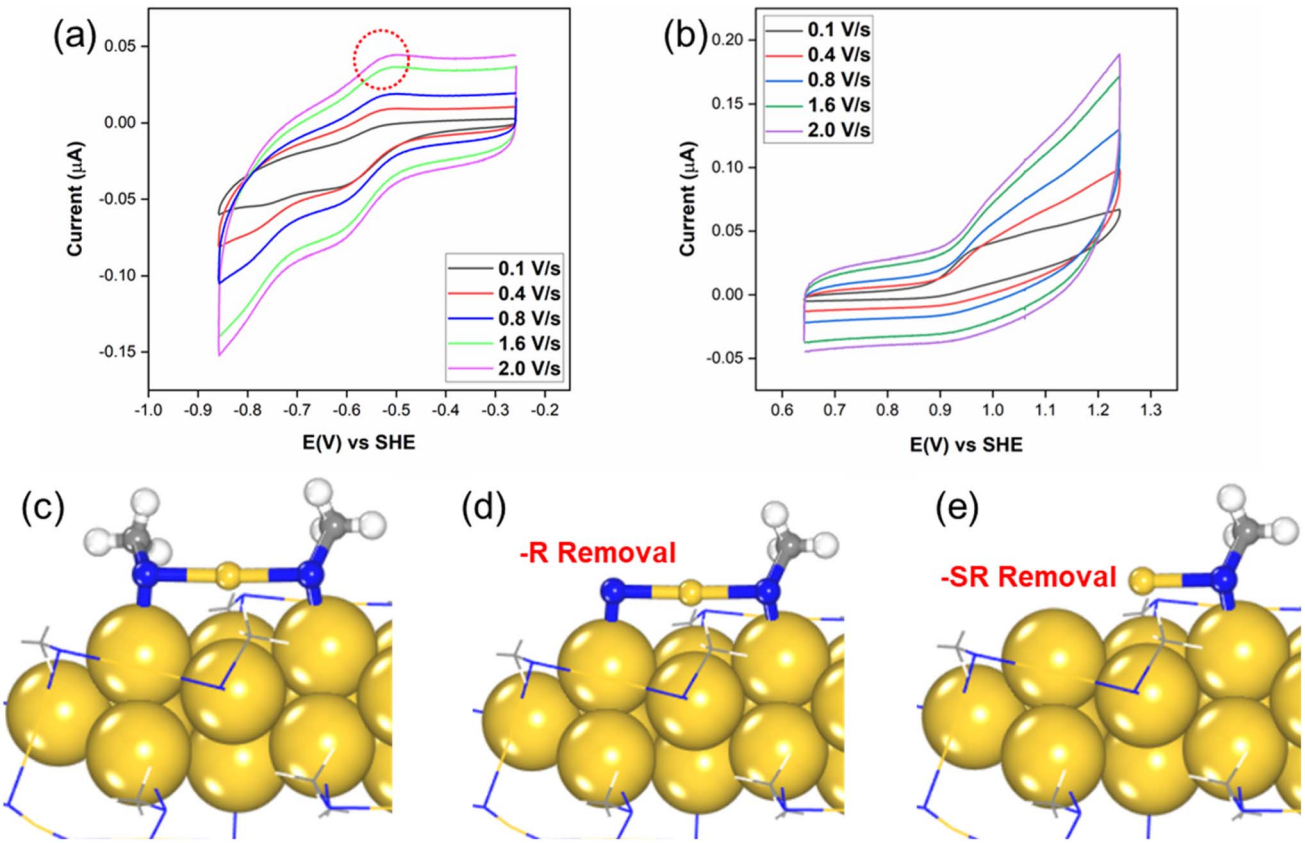


Fig. 2 CVs with narrower potential window around (a) LUMO and (b) HOMO region with different scan rates. Atomic structures of the $Au_{42}(SR)_{32}$ nanocluster in (c) fully ligand-protected, (d) –R removed, and (e) –SR removed configurations. Au atoms are shown in yellow, S in blue, C in gray, and H in white.

peak at about −0.5 V *vs.* RHE is absent in the first cycle but appears in later cycles. This is reminiscent of the reductive desorption of thiolates in 2D self-assembled monolayer from Au electrodes M-SR + $e^-$ → M-solvent + $RS_{solvated}^-$,[41,42] correspondingly the formation of active sites due to ligand removal reported in the prototype $Au_{25}$ nanoclusters,[40,43] a clear indication of *operando* ligand removal driven by electrode potential corroborating with the XPS results.

Motivated by this behavior, we investigate the role of ligand removal in modulating the nanocluster's catalytic activity. To encompass possible routes reported in literature,[44,45] we consider two ligand-removal scenarios: (1) detachment of the R-group from the thiolate ligand (–R removal, Fig. 2d), and (2) complete removal of the thiolate ligand (–SR removal, Fig. 2e). Under increasingly reductive potentials, –SR removal is expected to dominate *via* electrochemical protic attack on S atoms and reductive Au–S bond cleavage,[36] whereas –R removal, though thermodynamically feasible according to DFT, may only occur under more extreme conditions involving localized C–S bond polarization or radical-mediated scission. These ligand-modified, along with fully ligand-protected (Fig. 2c), nanocluster models are used in subsequent investigations of $CO_2$RR and HER activity to elucidate the effect of ligand dynamics on catalytic performance. In this work, we focus on configurations involving the removal of a single –R or –SR ligand to capture the initial stages of surface activation. Under more negative electrochemical potentials or extended electrolysis, however, additional ligands may be progressively detached, leading to partially or extensively deprotected cluster surfaces. Although modeling such multi-ligand removal events is computationally prohibitive due to the vast configurational space, the qualitative trends established here, particularly the identity of potential-determining steps and the relative order of activity among configurations, are expected to remain valid. Notably, XPS measurements (Fig. S5) reveal a gradual loss of thiolate species with increasing cathodic bias, supporting a stepwise ligand removal process. Future studies incorporating multiple-ligand removal scenarios will be important for understanding how progressive surface deprotection modifies the electronic structure and catalytic selectivity of these atomically precise nanoclusters under operating conditions.

Fig. 3 presents the free energy profiles for $CO_2$RR and HER on pristine, –R removed, and –SR removed $Au_{42}(SR)_{32}$ nanoclusters. For the pristine $Au_{42}(SR)_{32}$ nanocluster, the potential-determining step (PDS) is *COOH formation, with an onset potential of −2.15 V *vs.* RHE. Upon –R removal, the PDS shifts to *CO formation, although the onset potential remains comparable (−2.28 V *vs.* RHE). Notably, for the –SR removed nanocluster, the onset potential improves significantly to −0.47 V *vs.* RHE, while the PDS reverts to *COOH formation. HER profiles

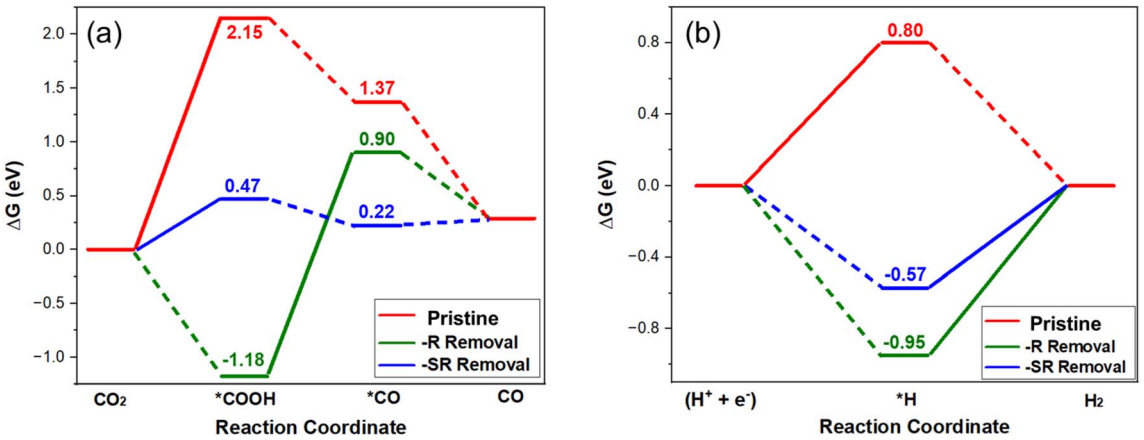


Fig. 3 Free energy profiles for (a) $CO_2$RR and (b) HER on pristine, –R removed, and –SR removed $Au_{42}(SR)_{32}$ nanoclusters. The potential-determining step (PDS) in each profile is indicated in bold.

also vary with ligand removal. The onset HER potentials for the pristine, –R removed, and –SR removed $Au_{42}(SR)_{32}$ nanoclusters are −0.80 V, −0.95 V, and −0.57 V *vs.* RHE, respectively. In the pristine nanocluster, the PDS is the adsorption of *H, whereas for the ligand-removed nanoclusters (–R or –SR), the PDS shifts to *H desorption. Overall, the –SR removed nanocluster exhibits the highest catalytic activity for both $CO_2$RR and HER, highlighting the critical role of ligand removal in enhancing catalytic performance. These findings align with previous studies on $Au_{25}$ nanoclusters, which have shown that fully ligand-protected nanoclusters exhibit low $CO_2$RR activity, and that localized ligand removal is essential to achieving high electrocatalytic performance.[40]

To gain mechanistic insight into how ligand removal affects catalytic activity, we analyzed the atomic structures associated with $CO_2$RR and HER on the three nanoclusters. Fig. 4 illustrates the active sites of $CO_2$RR for the pristine, –R removed, and –SR removed $Au_{42}(SR)_{32}$ nanoclusters (active sites of HER are shown in Fig. S6). For the pristine $Au_{42}(SR)_{32}$ nanocluster, the active site is located on the core Au. Due to the weak interaction with reaction intermediates, the PDS involves their adsorption (*COOH for $CO_2$RR and *H for HER), resulting in high onset potentials for both reactions. In the –R removed $Au_{42}(SR)_{32}$ nanocluster, the exposed and under-coordinated S atom serves as the active site. Here, the interaction with intermediates is excessively strong, making desorption the PDS and again leading to high onset potentials. In contrast, for the –SR removed nanocluster, the active sites shift to under-coordinated Au atoms, which exhibit moderate binding strength with reaction intermediates. This optimal interaction results in significantly enhanced activity for both $CO_2$RR and HER. Thus, changes in catalytic performance following ligand removal can be attributed to changes in the identity and coordination of the active sites, which modulate the binding affinity for key intermediates. Specifically, the –SR removed nanocluster, with under-coordinated Au active sites, provides the ideal balance in binding strength, thereby achieving superior catalytic activity. In comparison, the pristine and –R removed nanoclusters suffer from suboptimal binding, either too weak or too strong, which limits their catalytic performance.

We next explore the effects of Cu doping in the $Au_{42}(SR)_{32}$ nanocluster, as Cu is known to modify the electronic structure of Au-based systems and potentially enhance their catalytic performance for $CO_2$RR.[20,46,47] To systematically evaluate the impact of Cu incorporation, we examine all 42 possible single-dopant configurations of the $Au_{42}(SR)_{32}$ nanocluster, corresponding to Cu substitution at each individual Au site. The relative energies of these 42 isomers are listed in Table S1. Due to the symmetry of the $Au_{42}(SR)_{32}$ nanocluster, only eight of these configurations are symmetrically inequivalent. These distinct isomers are illustrated in Fig. S7, and their relative energies range from 0 to 0.23 eV, indicating a narrow thermodynamic distribution. Fig. 5a presents the most stable configuration, where the Cu dopant is substituted into the second metal layer (core region) of the nanocluster. The lowest-energy configuration with Cu located in the staple motif is shown in Fig. 5b, where the Cu atom occupies a site within the tetrameric staple motif. The energy difference between these two isomers is only 0.07 eV, suggesting that both configurations are thermodynamically accessible and may coexist under experimental conditions. Given their comparable stability, we investigate the $CO_2$RR and HER activity of both doped structures. The core-doped configuration is denoted as $Au_{41}Cu(A)$, while the staple-doped configuration is referred to as $Au_{41}Cu(B)$ in the following text.

Fig. 6a shows the free energy profiles for $CO_2$RR on the pristine, –R removed, and –SR removed $Au_{41}Cu(A)$ and $Au_{41}Cu(B)$ nanoclusters. For comparison, the profiles for the undoped $Au_{42}(SR)_{32}$ nanocluster are also included. The $CO_2$RR active sites for $Au_{41}Cu(A)$ and $Au_{41}Cu(B)$ are shown in Fig. S4 and S6, respectively. As expected, Cu doping enhances $CO_2$RR activity in the pristine nanoclusters (red lines in Fig. 6a), which can be attributed to the stronger binding of carbon-containing intermediates (*COOH and *CO), consistent with previous studies indicating that Cu doping generally promotes $CO_2$RR activity.[32,44,48] A similar enhancement is observed for the –R

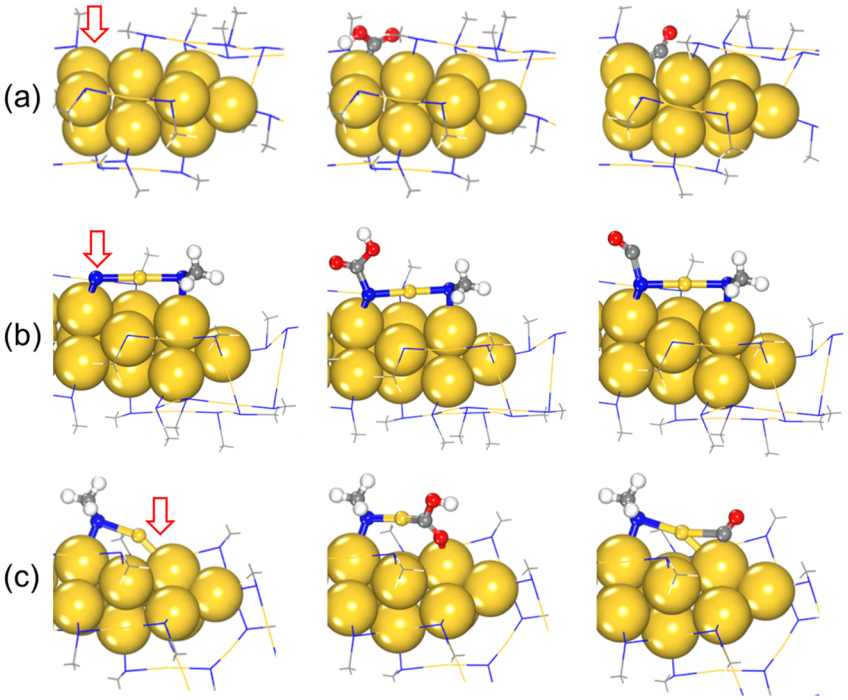


Fig. 4 Catalytically active sites for $CO_2RR$ on (a) the fully ligand-protected nanocluster, (b) the –R removed configuration, and (c) the –SR removed configuration. Au atoms are shown in yellow, S in blue, O in red, C in gray, and H in white.

removed nanoclusters (green lines in Fig. 6a); however, the underlying mechanism differs. In the undoped –R removed nanocluster, $CO_2RR$ is limited by overly strong binding of reaction intermediates. Cu doping appears to mitigate this by weakening the binding strength, likely due to stronger Cu–S bond compared to Au–S (Fig. S8 and S10), thereby improving $CO_2RR$ activity. Interestingly, Cu doping does not enhance $CO_2RR$ activity in the –SR removed nanoclusters, despite similarly increasing the binding of reaction intermediates. This unexpected behavior is due to a shift in the PDS: from *COOH formation in the undoped case to *CO desorption in the Cu-doped nanoclusters. As a result, stronger *CO binding hinders $CO_2RR$ activity in this configuration.

Fig. 6b presents the HER free energy profiles, and the corresponding HER active sites for $Au_{41}Cu$ (A) and $Au_{41}Cu$ (B) nanoclusters are shown in Fig. S5 and S7, respectively. In the pristine $Au_{42}(SR)_{32}$ nanocluster (red lines in Fig. 6b), Cu doping reduces HER activity due to weaker *H binding, along with the PDS being *H adsorption. For the –R removed nanocluster (green lines in Fig. 6b), although *H binding also weakens with Cu doping, HER activity increases. This is because the PDS in this case is *H desorption, which is facilitated by the weaker binding. In contrast, for the –SR removed nanoclusters (blue lines in Fig. 6b), HER activity is either slightly increased or decreased by Cu doping, depending on the dopant location. Overall, Cu doping enhances $CO_2RR$ activity while suppressing HER in both pristine and –R removed nanoclusters. In contrast, the –SR removed nanoclusters exhibit the opposite trend. These distinct behaviors arise from the fundamentally different nature of the active sites (Fig. S4–S7) and the resulting variations in binding affinities of key reaction intermediates influenced by Cu doping.

In addition to evaluating catalytic activity, we also assessed the selectivity between $CO_2RR$ and HER for the various $Au_{42}$-based nanoclusters. Previous studies have shown that the difference in limiting potentials for $CO_2RR$ and HER correlates

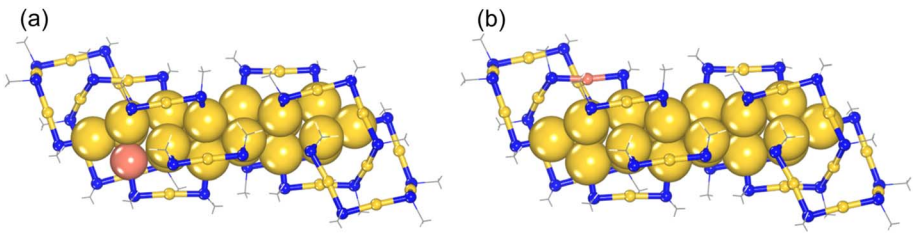


Fig. 5 The most stable Cu-doped $Au_{42}(SR)_{32}$ isomers: (a) core-doped and (b) staple-motif-doped configurations. Au atoms are shown in yellow, Cu in brown, S in blue, and C in gray.

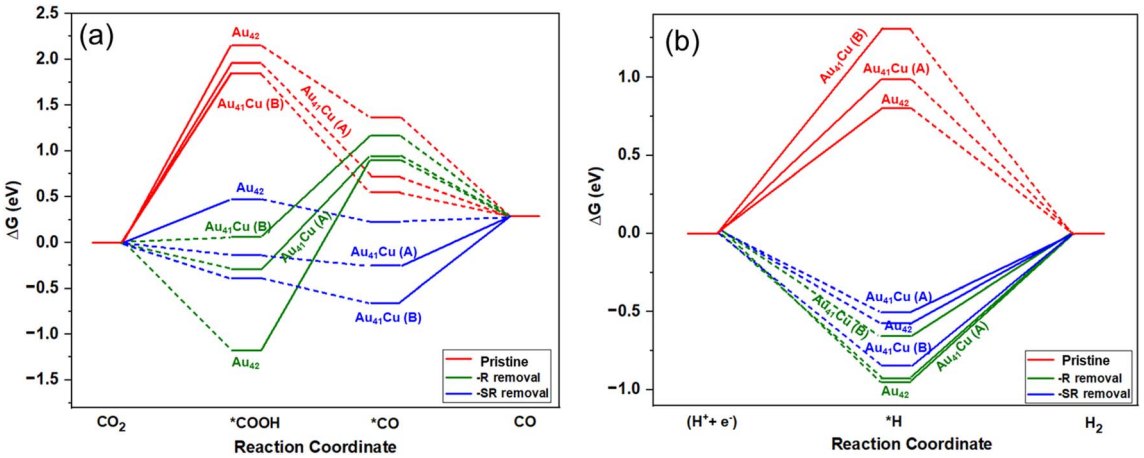


Fig. 6 Free energy profiles for (a) $CO_2$RR and (b) HER on pristine, −R removed, and −SR removed $Au_{41}Cu$(A) and $Au_{41}Cu$(B) nanoclusters. For comparison, the profiles for the undoped $Au_{42}(SR)_{32}$ nanocluster are also included. The PDS for each profile is highlighted in bold.

with selectivity: the most active and selective $CO_2$RR catalysts typically exhibit a low$|U_L(CO_2)|$ and a large $U_L(CO_2) - U_L(H_2)$ difference.[49] Fig. 7a summarizes both the activity and selectivity for the $Au_{42}$-based nanoclusters studied. In this plot, ideal catalysts appear in the upper right corner, combining high $CO_2$RR activity with strong selectivity over HER. Among the undoped $Au_{42}(SR)_{32}$ nanoclusters, the –SR removed configuration demonstrates the best performance for CO production. Cu doping enhances both activity and selectivity in the pristine and –R removed nanoclusters (indicated by red and green arrows, respectively), but it diminishes performance in the –SR removed configuration (blue arrow). These contrasting trends highlight the importance of considering the precise nature of ligand removal under operating conditions when interpreting catalytic behavior and optimizing performance through doping. The effects of doping can differ significantly between pristine and ligand-removed nanoclusters.

To further validate our findings, we experimentally evaluated the catalytic activity of the $Au_{42}(SR)_{32}$ nanocluster using heterogeneous electrochemical analysis. Fig. 7b shows the linear sweep voltammetry (LSV) data. Compared to the blank, *i.e.*, without $Au_{42}$ on the carbon paper electrode, under Ar purging, the increase in current density toward more negative potentials arises from HER as water is the only redox active species to be reduced. In $CO_2$-saturated solution, a sharp increase in reduction current was observed at lower potentials, indicating more facile $CO_2$ reduction over HER. The experimentally observed onset potentials (−0.54 V for $CO_2$RR and −0.69 V for HER) closely match the theoretical predictions for the –SR removed nanocluster, suggesting its relevance under *operando* conditions than the pristine and –R removed nanoclusters. It is also worth noting that the broad shoulder peak at around −0.4 to −0.6 V range coincides with the thiolate stripping of undoped $Au_{42}$ characterized experimentally by CV

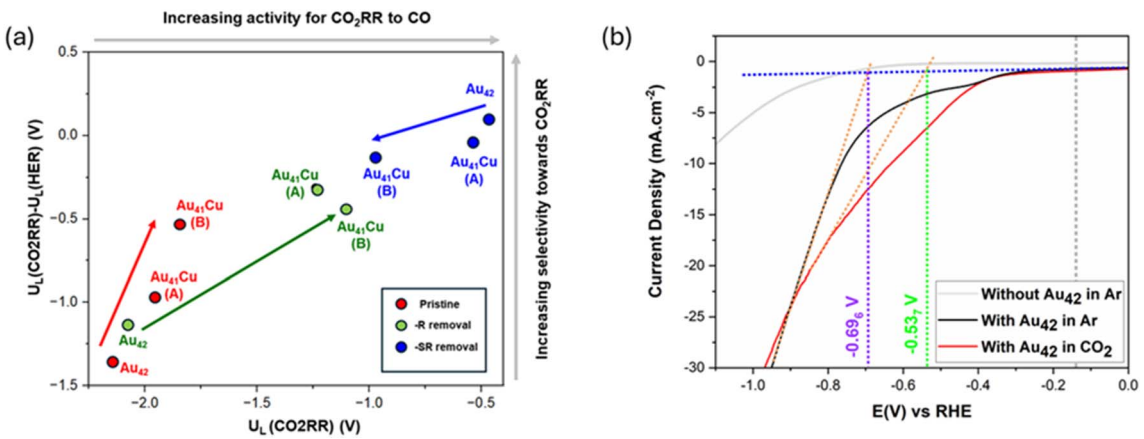


Fig. 7 (a) Activity *vs.* selectivity profiles for $Au_{42}$-based nanoclusters studied. Arrows show the trend on Cu doping for the pristine (red), −R removed (green), and −SR removed (blue) nanoclusters. (b) Linear sweep voltammograms of the $Au_{42}(SR)_{32}$ assembled on carbon paper as working electrode in Ar-saturated and $CO_2$ saturated electrolyte solution. The grey current curve is recorded without the $Au_{42}$ NCs but under otherwise identical conditions. Technical details about the onset potential determination and repeats showing consistency are provided in SI. For comparison, the gray dashed line at −0.14 V *vs.* RHE is added to represent the LUMO position at pH 7.2.

 

(Fig. S3), and the predicted HER of –SR removed onset potential. The low current density may indicate initial or limited active site(s) formation which require systematic studies underway, including combining constant-potential simulations with *operando* characterizations and product characterization to clarify the mechanism of ligand removal during catalysis, with the goal of achieving deeper insight and improved control over ligand detachment and the formation of active sites in nanoclusters.

## Conclusions

This work reveals the critical influence of ligand dynamics on the catalytic performance of the rod-shaped $Au_{42}(SR)_{32}$ nanoclusters. Our combined theoretical and experimental investigation shows that ligand removal significantly alters the electronic structure and active sites of the nanocluster, modulating both $CO_2$RR and HER activities. The –SR removed configuration stands out as the most active and selective for $CO_2$ reduction, attributable to the emergence of under-coordinated Au sites with optimal binding strengths. Cu doping is predicted to enhance catalytic performance in pristine and –R removed nanoclusters but reduces activity in the –SR removed case due to overly strong *CO binding and a shift in the potential-determining step. These contrasting trends emphasize the importance of understanding and controlling ligand-removal behavior under reaction conditions. Accurately identifying *operando* active sites is essential for the rational design of doped APNCs with high catalytic efficiency and selectivity for $CO_2$RR.

## Author contributions

R. S. and A. S. performed the DFT calculations, electrochemical analysis, and data interpretation involved in this study. L. L. and R. J. synthesized the nanoclusters and assisted in structural and spectroscopic characterization. G. W. and G. H. conceptualized the research, guided the experimental and theoretical work, and supervised the project. G. H. also led the preparation of the manuscript. All authors contributed to the discussion and revision of the manuscript.

## Conflicts of interest

There are no conflicts to declare.

## Data availability

The data supporting this article have been included as part of the supplementary information (SI). Supplementary information is available. See DOI: https://doi.org/10.1039/d5ta05852j.

## Acknowledgements

This article is based on work supported as part of the Atomic-C2E project by the U.S. Department of Energy, Office of Science under award number DE-SC-0024716. This research used resources of the National Energy Research Scientific Computing Center, a DOE Office of Science User Facility supported by the Office of Science of the U.S. Department of Energy under contract no. DE-AC02-05CH11231 using NERSC award BES-ERCAP0032102.

## References

1 J. Artz, T. E. Müller, K. Thenert, J. Kleinekorte, R. Meys, A. Sternberg, A. Bardow and W. Leitner, Sustainable Conversion of Carbon Dioxide: An Integrated Review of Catalysis and Life Cycle Assessment, *Chem. Rev.*, 2018, **118**(2), 434–504, DOI: 10.1021/acs.chemrev.7b00435.

2 D. T. Whipple and P. J. A. Kenis, Prospects of CO2 Utilization via Direct Heterogeneous Electrochemical Reduction, *J. Phys. Chem. Lett.*, 2010, **1**(24), 3451–3458, DOI: 10.1021/jz1012627.

3 G. Centi, E. Alessandra Quadrelli and S. Perathoner, Catalysis for CO 2 Conversion: A Key Technology for Rapid Introduction of Renewable Energy in the Value Chain of Chemical Industries, *Energy Environ. Sci.*, 2013, **6**(6), 1711–1731, DOI: 10.1039/C3EE00056G.

4 M. Peters, B. Köhler, W. Kuckshinrichs, W. Leitner, P. Markewitz and T. E. Müller, Chemical Technologies for Exploiting and Recycling Carbon Dioxide into the Value Chain, *ChemSusChem*, 2011, **4**(9), 1216–1240, DOI: 10.1002/cssc.201000447.

5 P. Saha, S. Amanullah and A. Dey, Selectivity in Electrochemical CO2 Reduction, *Acc. Chem. Res.*, 2022, **55**(2), 134–144, DOI: 10.1021/acs.accounts.1c00678.

6 C. Costentin, M. Robert and J.-M. Savéant, Catalysis of the Electrochemical Reduction of Carbon Dioxide, *Chem. Soc. Rev.*, 2013, **42**(6), 2423–2436, DOI: 10.1039/C2CS35360A.

7 Y. Lu and W. Chen, Sub-Nanometre Sized Metal Clusters: From Synthetic Challenges to the Unique Property Discoveries, *Chem. Soc. Rev.*, 2012, **41**(9), 3594–3623, DOI: 10.1039/C2CS15325D.

8 K. Kwak and D. Lee, Electrochemistry of Atomically Precise Metal Nanoclusters, *Acc. Chem. Res.*, 2019, **52**(1), 12–22, DOI: 10.1021/acs.accounts.8b00379.

9 W. Jing, H. Shen, R. Qin, Q. Wu, K. Liu and N. Zheng, Surface and Interface Coordination Chemistry Learned from Model Heterogeneous Metal Nanocatalysts: From Atomically Dispersed Catalysts to Atomically Precise Clusters, *Chem. Rev.*, 2023, **123**(9), 5948–6002, DOI: 10.1021/acs.chemrev.2c00569.

10 G. Li and R. Jin, Atomically Precise Gold Nanoclusters as New Model Catalysts, *Acc. Chem. Res.*, 2013, **46**(8), 1749–1758, DOI: 10.1021/ar300213z.

11 Y. Du, H. Sheng, D. Astruc and M. Zhu, Atomically Precise Noble Metal Nanoclusters as Efficient Catalysts: A Bridge between Structure and Properties, *Chem. Rev.*, 2020, **120**(2), 526–622, DOI: 10.1021/acs.chemrev.8b00726.

12 J. Yan, B. K. Teo and N. Zheng, Surface Chemistry of Atomically Precise Coinage–Metal Nanoclusters: From Structural Control to Surface Reactivity and Catalysis, *Acc. Chem. Res.*, 2018, **51**(12), 3084–3093, DOI: 10.1021/acs.accounts.8b00371.

13 R. Jin, G. Li, S. Sharma, Y. Li and X. Du, Toward Active-Site Tailoring in Heterogeneous Catalysis by Atomically Precise Metal Nanoclusters with Crystallographic Structures, *Chem. Rev.*, 2021, **121**(2), 567–648, DOI: 10.1021/acs.chemrev.0c00495.

14 Q. Tang, G. Hu, V. Fung and D. Jiang, Insights into Interfaces, Stability, Electronic Properties, and Catalytic Activities of Atomically Precise Metal Nanoclusters from First Principles, *Acc. Chem. Res.*, 2018, **51**(11), 2793–2802, DOI: 10.1021/acs.accounts.8b00380.

15 R. Jin, C. Zeng, M. Zhou and Y. Chen, Atomically Precise Colloidal Metal Nanoclusters and Nanoparticles: Fundamentals and Opportunities, *Chem. Rev.*, 2016, **116**(18), 10346–10413, DOI: 10.1021/acs.chemrev.5b00703.

16 X. Liu, X. Cai and Y. Zhu, Catalysis Synergism by Atomically Precise Bimetallic Nanoclusters Doped with Heteroatoms, *Acc. Chem. Res.*, 2023, **56**(12), 1528–1538, DOI: 10.1021/acs.accounts.3c00118.

17 X. Du and R. Jin, Atomic-Precision Engineering of Metal Nanoclusters, *Dalton Trans.*, 2020, **49**(31), 10701–10707, DOI: 10.1039/D0DT01853H.

18 A. Ghosh, O. F. Mohammed and O. M. Bakr, Atomic-Level Doping of Metal Clusters, *Acc. Chem. Res.*, 2018, **51**(12), 3094–3103, DOI: 10.1021/acs.accounts.8b00412.

19 Y. Li, M. Zhou and R. Jin, Programmable Metal Nanoclusters with Atomic Precision, *Adv. Mater.*, 2021, **33**(46), 2006591, DOI: 10.1002/adma.202006591.

20 Y. Negishi, K. Munakata, W. Ohgake and K. Nobusada, Effect of Copper Doping on Electronic Structure, Geometric Structure, and Stability of Thiolate-Protected Au25 Nanoclusters, *J. Phys. Chem. Lett.*, 2012, **3**(16), 2209–2214, DOI: 10.1021/jz300892w.

21 S. Hossain, D. Hirayama, A. Ikeda, M. Ishimi, S. Funaki, A. Samanta, T. Kawawaki and Y. Negishi, Atomically Precise Thiolate-Protected Gold Nanoclusters: Current Status of Designability of the Structure and Physicochemical Properties, *Aggregate*, 2023, **4**(2), e255, DOI: 10.1002/agt2.255.

22 D. R. Kauffman, D. Alfonso, C. Matranga, H. Qian and R. Jin, Experimental and Computational Investigation of Au25 Clusters and CO2: A Unique Interaction and Enhanced Electrocatalytic Activity, *J. Am. Chem. Soc.*, 2012, **134**(24), 10237–10243, DOI: 10.1021/ja303259q.

23 S. Zhao, R. Jin and R. Jin, Opportunities and Challenges in $CO_2$ Reduction by Gold- and Silver-Based Electrocatalysts: From Bulk Metals to Nanoparticles and Atomically Precise Nanoclusters, *ACS Energy Lett.*, 2018, **3**(2), 452–462, DOI: 10.1021/acsenergylett.7b01104.

24 Y. Li, Y. Song, X. Zhang, T. Liu, T. Xu, H. Wang, D. Jiang and R. Jin, Atomically Precise Au42 Nanorods with Longitudinal Excitons for an Intense Photothermal Effect, *J. Am. Chem. Soc.*, 2022, **144**(27), 12381–12389, DOI: 10.1021/jacs.2c03948.

25 A. Peterson, F. Abild-Pedersen, F. Studt, J. Rossmeisl and K. Nørskov, How Copper Catalyzes the Electroreduction of Carbon Dioxide into Hydrocarbon Fuels, *Energy Environ. Sci.*, 2010, **3**(9), 1311–1315, DOI: 10.1039/C0EE00071J.

26 C.-T. Dinh, T. Burdyny, M. G. Kibria, A. Seifitokaldani, C. M. Gabardo, F. P. García de Arquer, A. Kiani, J. P. Edwards, P. De Luna, O. S. Bushuyev, C. Zou, R. Quintero-Bermudez, Y. Pang, D. Sinton and E. H. Sargent, CO2 Electroreduction to Ethylene via Hydroxide-Mediated Copper Catalysis at an Abrupt Interface, *Science*, 2018, **360**(6390), 783–787, DOI: 10.1126/science.aas9100.

27 H. Li, T. Liu, P. Wei, L. Lin, D. Gao, G. Wang and X. Bao, High-Rate CO2 Electroreduction to C2+ Products over a Copper-Copper Iodide Catalyst, *Angew. Chem., Int. Ed.*, 2021, **60**(26), 14329–14333, DOI: 10.1002/anie.202102657.

28 W. Ma, S. Xie, T. Liu, Q. Fan, J. Ye, F. Sun, Z. Jiang, Q. Zhang, J. Cheng and Y. Wang, Electrocatalytic Reduction of CO2 to Ethylene and Ethanol through Hydrogen-Assisted C–C Coupling over Fluorine-Modified Copper, *Nat. Catal.*, 2020, **3**(6), 478–487, DOI: 10.1038/s41929-020-0450-0.

29 B. Wu, J. Chen and L. Qian, Recent Advances in Heterogeneous Electroreduction of CO2 on Copper-Based Catalysts, *Catalysts*, 2022, **12**(8), 860, DOI: 10.3390/catal12080860.

30 D. Kim, C. Xie, N. Becknell, Y. Yu, M. Karamad, K. Chan, E. J. Crumlin, J. K. Nørskov and P. Yang, Electrochemical Activation of CO2 through Atomic Ordering Transformations of AuCu Nanoparticles, *J. Am. Chem. Soc.*, 2017, **139**(24), 8329–8336, DOI: 10.1021/jacs.7b03516.

31 Y. Yang, S. Louisia, S. Yu, J. Jin, I. Roh, C. Chen, M. V. Fonseca Guzman, J. Feijóo, P.-C. Chen, H. Wang, C. J. Pollock, X. Huang, Y.-T. Shao, C. Wang, D. A. Muller, H. D. Abruña and P. Yang, Operando Studies Reveal Active Cu Nanograins for CO2 Electroreduction, *Nature*, 2023, **614**(7947), 262–269, DOI: 10.1038/s41586-022-05540-0.

32 G. Deng, H. Yun, M. S. Bootharaju, F. Sun, K. Lee, X. Liu, S. Yoo, Q. Tang, Y. J. Hwang and T. Hyeon, Copper Doping Boosts Electrocatalytic CO2 Reduction of Atomically Precise Gold Nanoclusters, *J. Am. Chem. Soc.*, 2023, **145**(50), 27407–27414, DOI: 10.1021/jacs.3c08438.

33 R. Jin and K. Nobusada, Doping and Alloying in Atomically Precise Gold Nanoparticles, *Nano Res.*, 2014, **7**(3), 285–300, DOI: 10.1007/s12274-014-0403-5.

34 S. Li, W. Tian and Y. Liu, The Ligand Effect of Atomically Precise Gold Nanoclusters in Tailoring Catalytic Properties, *Nanoscale*, 2021, **13**(40), 16847–16859, DOI: 10.1039/D1NR05232B.

35 X.-K. Wan, J.-Q. Wang, Z.-A. Nan and Q.-M. Wang, Ligand Effects in Catalysis by Atomically Precise Gold Nanoclusters, *Sci. Adv.*, 2017, **3**(10), e1701823, DOI: 10.1126/sciadv.1701823.

36 F. Sun, L. Qin, Z. Tang, G. S. Deng, M. Bootharaju, Z. Wei, Q. Tang and T. Hyeon, SR Removal or –R Removal? A Mechanistic Revisit on the Puzzle of Ligand Etching of Au 25 (SR) 18 Nanoclusters during Electrocatalysis, *Chem. Sci.*, 2023, **14**(38), 10532–10546, DOI: 10.1039/D3SC03018K.

37 D. García-Raya, R. Madueño, M. Blázquez and T. Pineda, Electrochemistry of Molecule-like Au25 Nanoclusters Protected by Hexanethiolate, *J. Phys. Chem. C*, 2009, **113**(20), 8756–8761, DOI: 10.1021/jp901118t.

38 S. Antonello, N. V. Perera, M. Ruzzi, J. A. Gascón and F. Maran, Interplay of Charge State, Lability, and Magnetism in the Molecule-like Au25(SR)18 Cluster, *J. Am. Chem. Soc.*, 2013, **135**(41), 15585–15594, DOI: 10.1021/ja407887d.

39 K. G. Stamplecoskie, Y.-S. Chen and P. V. Kamat, Excited-State Behavior of Luminescent Glutathione-Protected Gold Clusters, *J. Phys. Chem. C*, 2014, **118**(2), 1370–1376, DOI: 10.1021/jp410856h.

40 H. Seong, V. Efremov, G. Park, H. Kim, J. S. Yoo and D. Lee, Atomically Precise Gold Nanoclusters as Model Catalysts for Identifying Active Sites for Electroreduction of CO2, *Angew. Chem.*, 2021, **133**(26), 14684–14691, DOI: 10.1002/ange.202102887.

41 R. C. Salvarezza and P. Carro, The Electrochemical Stability of Thiols on Gold Surfaces, *J. Electroanal. Chem.*, 2018, **819**, 234–239, DOI: 10.1016/j.jelechem.2017.10.046.

42 N. C. Ramos, J. W. Medlin and A. Holewinski, Electrochemical Stability of Thiolate Self-Assembled Monolayers on Au, Pt, and Cu, *ACS Appl. Mater. Interfaces*, 2023, **15**(11), 14470–14480, DOI: 10.1021/acsami.3c01224.

43 N. Austin, S. Zhao, J. R. McKone, R. Jin and G. Mpourmpakis, Elucidating the Active Sites for CO2 Electroreduction on Ligand-Protected Au25 Nanoclusters, *Catal. Sci. Technol.*, 2018, **8**(15), 3795–3805, DOI: 10.1039/C8CY01099D.

44 S. Li, A. V. Nagarajan, D. R. Alfonso, M. Sun, D. R. Kauffman, G. Mpourmpakis and R. Jin, Boosting CO2 Electrochemical Reduction with Atomically Precise Surface Modification on Gold Nanoclusters, *Angew. Chem., Int. Ed.*, 2021, **60**(12), 6351–6356, DOI: 10.1002/anie.202016129.

45 D. R. Alfonso, D. Kauffman and C. Matranga, Active Sites of Ligand-Protected Au25 Nanoparticle Catalysts for CO2 Electroreduction to CO, *J. Chem. Phys.*, 2016, **144**(18), 184705, DOI: 10.1063/1.4948792.

46 G. Hu, Q. Tang, D. Lee, Z. Wu and D. Jiang, Metallic Hydrogen in Atomically Precise Gold Nanoclusters, *Chem. Mater.*, 2017, **29**(11), 4840–4847, DOI: 10.1021/acs.chemmater.7b00776.

47 S. M. Lang, P. Claes, N. T. Cuong, M. T. Nguyen, P. Lievens and E. Janssens, Copper Doping of Small Gold Cluster Cations: Influence on Geometric and Electronic Structure, *J. Chem. Phys.*, 2011, **135**(22), 224305, DOI: 10.1063/1.3664307.

48 E. Ibáñez-Alé, J. Hu, J. Albero, L. Simonelli, C. Marini, N. López, N. Barrabés, H. García and S. Goberna-Ferrón, Structural Evolution of Stapes Controls the Electrochemical CO2 Reduction on Bimetallic Cu-Doped Gold Nanoclusters, *Small*, 2025, **21**(2), 2408531, DOI: 10.1002/smll.202408531.

49 P. Saha, S. Amanullah and A. Dey, Selectivity in Electrochemical CO2 Reduction, *Acc. Chem. Res.*, 2022, **55**(2), 134–144, DOI: 10.1021/acs.accounts.1c00678.